

Calibration of the AKARI Far-Infrared Imaging Fourier Transform Spectrometer

Noriko MURAKAMI^{1,2}, Mitsunobu KAWADA^{2,4}, Hidenori TAKAHASHI³, Yoko OKADA^{4,5}, Akiko YASUDA^{2,4}, Takafumi OOTSUBO^{4,6}, Hidehiro KANEDA², Hiroshi MATSUO⁷, Jean-Paul BALUTEAU⁸, Peter DAVIS-IMHOF⁹, Brad G. GOM¹⁰, David A. NAYLOR¹¹, Annie ZAVAGNO⁸, Issei YAMAMURA⁴, Shuji MATSUURA⁴, Mai SHIRAHATA⁴, Yasuo DOI¹², Takao NAKAGAWA⁴, and Hiroshi SHIBAI¹³

¹*Bisei Astronomical Observatory, 1723-70 Okura, Bisei-cho, Ibara-shi, Okayama 714-1411, Japan
noriko@bao.go.jp*

²*Graduate School of Sciences, Nagoya University, Furo-cho, Chikusa-ku, Nagoya 464-8602, Japan
kawada@u.phys.nagoya-u.ac.jp*

³*Gunma Astronomical Observatory, 6860-86 Nakayama, Takayama, Agatsuma, Gunma 377-0702, Japan*

⁴*Institute of Space and Astronautical Science, JAXA, 3-1-1 Yoshinodai, Chuo-ku, Sagami-hara 252-5210, Japan*

⁵*I. Physikalisches Institut, Universität zu Köln, Zùlpicher Str. 77, 50937 Köln, Germany*

⁶*Astronomical Institute, Graduate School of Science, Tohoku university, Aramaki, Aoba-ku, Sendai, 980-8578, Japan*

⁷*Advanced Technology Center, National Astronomical Observatory of Japan, 2-21-1 Osawa, Mitaka, Tokyo 181-8588, Japan*

⁸*Laboratoire d'Astrophysique de Marseille, UMR 6110 CNRS & Universite de Provence, 13388 Marseille Cedex 13, France*

⁹*Blue Sky Spectroscopy Inc., 9-740 4th Avenue South, Lethbridge, T1J 0N9, Alberta, Canada*

¹⁰*University of Lethbridge, Lethbridge T1K 3M4, Alberta, Canada*

¹¹*Institute for Space Imaging Science, University of Lethbridge, Lethbridge T1K 3M4, Alberta, Canada*

¹²*Department of General System Studies, Graduate School of Arts and Sciences, The University of Tokyo, 3-8-1 Komaba, Meguro-ku, Tokyo 153-8902, Japan*

¹³*Graduate School of Sciences, Osaka University, 1-1 Machikaneyama, Toyonaka, Osaka 560-0043, Japan*

(Received 2010 March 14; accepted 2010 June 14)

Abstract

The Far-Infrared Surveyor (FIS) onboard the AKARI satellite has a spectroscopic capability provided by a Fourier transform spectrometer (FIS-FTS). FIS-FTS is the

first space-borne imaging FTS dedicated to far-infrared astronomical observations. We describe the calibration process of the FIS-FTS and discuss its accuracy and reliability. The calibration is based on the observational data of bright astronomical sources as well as two instrumental sources. We have compared the FIS-FTS spectra with the spectra obtained from the Long Wavelength Spectrometer (LWS) of the Infrared Space Observatory (ISO) having a similar spectral coverage. The present calibration method accurately reproduces the spectra of several solar system objects having a reliable spectral model. Under this condition the relative uncertainty of the calibration of the continuum is estimated to be $\pm 15\%$ for SW, $\pm 10\%$ for 70–85 cm^{-1} of LW, and $\pm 20\%$ for 60–70 cm^{-1} of LW; and the absolute uncertainty is estimated to be $+35/-55\%$ for SW, $+35/-55\%$ for 70–85 cm^{-1} of LW, and $+40/-60\%$ for 60–70 cm^{-1} of LW. These values are confirmed by comparison with theoretical models and previous observations by the ISO/LWS.

Key words: instrumentation: spectrometer - methods: data analysis - space vehicles: instruments - infrared: general

1. Introduction

Since the Earth’s atmosphere is opaque at far-infrared wavelengths, we have to use air- or space-borne instruments for observing the universe at these wavelengths. In the last few decades, developments in infrared and space technologies have provided great opportunities to astronomers. In 1983, the first infrared astronomical satellite, IRAS (Neugebauer et al. 1984), provided the first view of the infrared universe. Following the success of this pioneering mission, the first Japanese infrared astronomical mission, InfraRed Telescope in Space (IRTS; Murakami et al. 1996) and the European Infrared Space Observatory (ISO; Kessler et al. 1996) were operated in the late 1990s. These missions extended the photometric observations by IRAS to spectroscopic measurements, which provided a new and powerful tool for probing astronomical properties.

The far-infrared spectral region is dominated by thermal emission of the interstellar dust and some prominent atomic fine structure lines, such as [C II] (63.4 cm^{-1} , 158 μm), [N II] (82.1 cm^{-1} , 122 μm) and [O III] (113.2 cm^{-1} , 88 μm). The spectral lines indicate the physical properties of the interstellar medium. For example, the [C II] line is a major cooling line in the photo-dissociation regions (PDRs; Tielens & Hollenbach 1985) and was detected around the Galactic Plane and nearby galaxies. The Far-Infrared Absolute Spectrophotometer (FIRAS; Mather et al. 1993b), mounted on the Cosmic Background Explorer (COBE; Mather 1993a, launched in 1983) detected the line/continuum emission from the interstellar gas/dust of the Galaxy as well as the cosmic microwave background radiation (Mather et al. 1990). The Far-

Infrared Line Mapper (FILM) onboard IRTS surveyed the [C II] line with high sensitivity; however, the surveyed area was limited to 7% of the entire sky (Shibai et al. 1996). Two balloon-borne telescopes, the Balloon-borne Infrared Telescope (BIRT) and the Balloon-borne Infrared Carbon Explorer (BICE), efficiently mapped the Galactic Plane with the same line (Shibai et al. 1991, Nakagawa et al. 1995). A rocket-borne instrument detected the same line in the Lockman Hole region with very high sensitivity (Bock et al. 1994, Matsuhara et al. 1997). Unfortunately, after the expiration of the Long Wavelength Spectrometer of ISO (LWS; Clegg et al. 1996) there were no space-based facilities for far-infrared spectroscopy. The Spitzer Space Telescope (SST; Werner et al. 2004) has been extremely productive for infrared astronomy; however it lacks a far-infrared spectroscopic capability.

The Japanese infrared astronomical satellite AKARI (Murakami et al. 2007) was launched in February 22, 2006 (JST). One of the two focal-plane instruments is the Far-Infrared Surveyor (FIS; Kawada et al. 2007). The primary purpose of the FIS was to accomplish a fine, unbiased photometric survey of the entire sky in four photometric bands covering the wavenumber range from 55 cm^{-1} to 200 cm^{-1} . In addition, the FIS also has a slow-scan observation mode (Shirahata et al. 2009) and a spectroscopic observation mode provided by a Fourier transform spectrometer (FIS-FTS). FIS-FTS is a Martin-Puplett type interferometer (Martin & Puplett 1969) and is similar in optical design to the composite infrared spectrometer (CIRS; Kunde et al. 1996) on the Cassini satellite. A unique feature of the FIS-FTS is its detector system. Two sets of two-dimensional photoconductive detector arrays are installed at both the output ports of the interferometer, providing an imaging spectroscopic capability. Therefore, the FIS-FTS is the first imaging FTS for far-infrared astronomy in space. The principal advantage of the FIS-FTS over the ISO/LWS is the high observational efficiency due to its imaging capability. The SPIRE instrument (Griffin et al. 2008) of the Herschel Space Observatory (Pilbratt 2008), launched in May 2009, also contains an imaging FTS and provides fine spectral images of the submillimeter sky ¹.

The FIS-FTS performance in space was generally consistent with that expected before launch laboratory tests. The instrument had worked well until the loss of its liquid helium on August 26, 2007 rendered the detectors inoperative. During the on-orbit operation of one and a half years, the FIS-FTS achieved 600 pointed observations. One of the challenges in analyzing the FIS-FTS data is the unique issues that arise from using photoconductive detector arrays in conjunction with an FTS. In this paper, we describe how the incident spectra are reproduced from the measured signals and discuss the accuracy and reliability of the calibration. The next section introduces the essential points about the instrument and its operation. In section 3, FIS-FTS standard data processing is reviewed briefly. Section 4 and 5 describe the calibration methods of spectral flux and wavenumber scale, respectively. The uncertainty of the calibration is summarized in section 6. In section 7, the reliability of this calibration method is discussed

¹ Herschel Science demonstration workshop - http://herschel.esac.esa.int/SDP_DP_wkshop.shtml

Table 1. The specifications of FIS-FTS.

detector unit	SW	LW
Spectral Coverage*	85 – 130 cm ⁻¹	60 – 88 cm ⁻¹
Array format	3 × 20	3 × 15
Pixel scale	26''8	44''2
FWHM(major/minor)	44'' / 39''	57'' / 53''
Sampling rate	170.66 Hz	85.33 Hz
operation mode	SED mode	full-res. mode
OPD range (L)	±0.42 cm	-0.9 ~ +2.7 cm
Resolution (1/2L _{max})	1.2 cm ⁻¹	0.18 cm ⁻¹
Mirror scan speed	~ 0.073 cm s ⁻¹	~ 0.076 cm s ⁻¹

* effective spectral coverage in this calibration.

by exploring available cross-calibration data. Some scientific results using this calibration are discussed by Yasuda et al. (2008), Okada et al. (2009) and Takahashi et al. (in preparation).

2. Instrument and Operation Sequence

2.1. Instrument

FIS-FTS has two types of detector arrays covering the wavenumber range from 55 to 200 cm⁻¹. The longer wavelength array, LW (Doi et al. 2002), is a compact stressed Ge:Ga array detector and the shorter wavelength array, SW (Fujiwara et al. 2003), is a monolithic Ge:Ga array detector. Both the LW and SW arrays have two parts in the arrays, corresponding to wider bands (three rows) and narrower bands (two rows), respectively, for photometric observations. FIS-FTS uses only the wider band part (three rows) of each detector array (see figure 3 in Kawada et al. 2007).

The optical design of the FIS-FTS is described in Kawada et al. (2008). Here, we summarize it. The convergent beam from the telescope is collimated after the bending mirror (see figure 1). The collimated beam passes through the low-pass filters to block photons shorter than 30 μm. The linearly polarized beam produced by the input polarizer is divided into two beams by a polarizing beam splitter. One of the two beams is reflected by the fixed roof-top mirror and the other is reflected by the moving roof-top mirror that changes the optical path difference (OPD) between the two beams. After reflection by the roof-top mirrors, the two beams recombine at the polarizing beam splitter. Finally, the output polarizer directs the two orthogonal components of the output beam to the two detector arrays. FIS-FTS uses a polarizing beam splitter instead of a dichroic beam splitter. Therefore, each detector array receives a complementary interference signal, i.e. when one array observes a bright central burst (peak), the other array observes a dark central burst (valley).

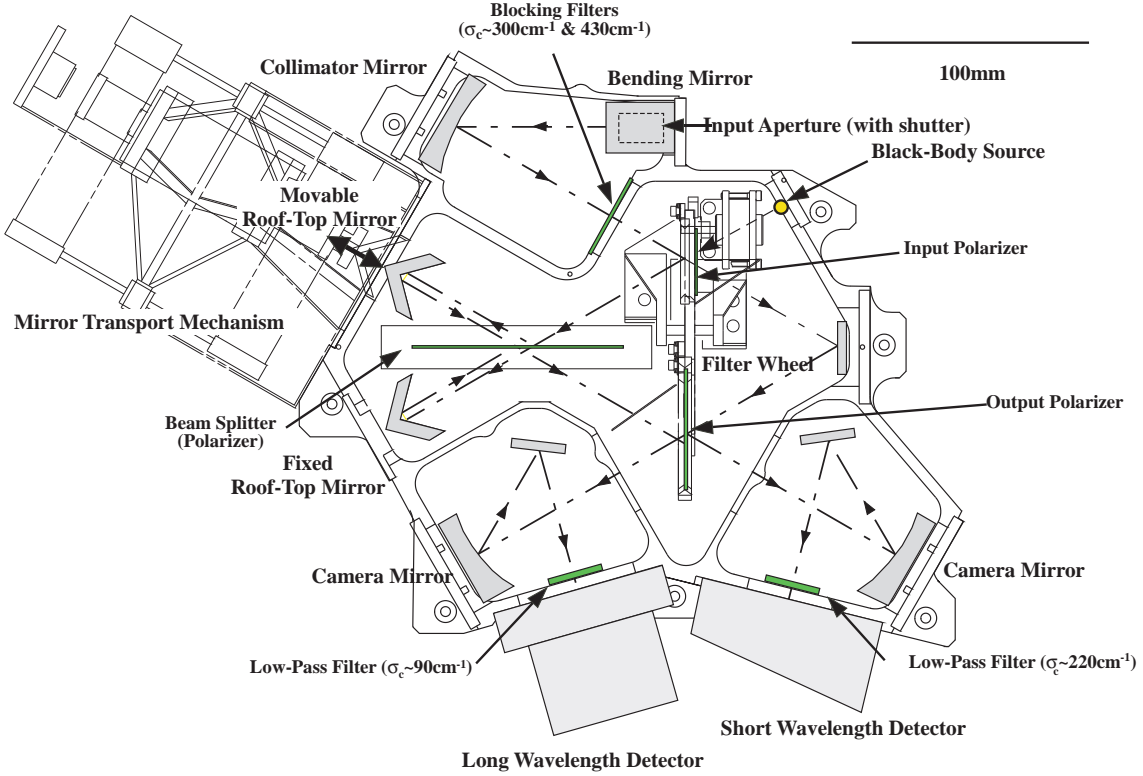


Fig. 1. Optical design of the FIS-FTS

A small blackbody source is installed on the opposite side of the input polarizer for monitoring the responsivity change. The temperature of this source can be changed up to 50K. The key features of the FIS-FTS are listed in table 1.

2.2. Operation Sequence

Astronomical observations using the FIS instrument are performed according to the astronomical observation templates (AOTs) of AKARI (see Kawada et al. 2007, AKARI FIS Data Users Manual²). The AOT labeled FIS03 is dedicated for observation using the FIS-FTS. FIS03 is one of the pointed observation modes of the satellite and the duration is 30 minutes including the attitude maneuver operation of the satellite. During the attitude maneuver from the all-sky survey mode to the pointed observation mode, the spectra of the internal blackbody source stabilized at 38K are measured with the shutter closed. Once the satellite attitude becomes stable, the cold shutter opens and the observation starts. After 12 minutes observation, the cold shutter is closed again and the maneuver from the pointed observation mode to the all-sky survey mode is executed.

FIS-FTS has two spectral resolution operation modes: a higher resolution mode (resolution = 0.18cm^{-1}) called the “full-resolution mode” and a lower resolution mode (resolution

² AKARI (ASTRO-F) Observers Page - <http://www.ir.isas.jaxa.jp/ASTRO-F/Observation/>

$= 1.2\text{cm}^{-1}$) called the “spectral energy distribution mode” (SED mode) (table 1). Each mode is selected by changing the scan length of the moving mirror. The mirror scan speeds of both modes are similar. Selectable parameters of FIS03 are the spectral resolution (full-resolution mode or SED mode), the reset interval of the detector readout electronics, and the on-source position on the detector arrays. We have three choices for the last parameter: the center of the SW array, the center of the LW array, or the center of the overlapped area of two arrays.

All measurements of the internal blackbody source are performed with the SED mode and a reset interval of 0.5 seconds. Before opening the cold shutter, the parameters are set to the selected values for each target. The detector signals and the OPD of the interferometer are acquired simultaneously and recorded. The data are sampled at a constant time interval. The sampling rate of the SW array is twice of LW (table 1).

3. Standard Data Processing

The data analysis flow of FIS-FTS taken with FIS03 is as follows:

1. Generation of interferograms by combining the detector signals with the OPD
2. Calculation of spectra by discrete Fourier transformation of the interferograms
3. Corrections to obtain the spectra of the objects

This sequence is shown in figure 2. These procedures are involved in the FIS-FTS data processing pipeline (AKARI FTS Toolkit Manual³) as the standard process. Each step is described separately in the following subsections.

3.1. Generation of Interferograms

The far-infrared detector signals are read out using the integration amplifier circuit. After correction for the non-linearity of the readout electronics (see AKARI FIS Data Users Manual), the data are differentiated one by one with the time-sequential signals sampled with a constant interval. Glitches caused by charged particles striking the detector or electronics (Suzuki et al. 2008) are removed from the signals at this stage. The sampling interval in the OPD depends on the scanning speed of the moving mirror. The speed of the moving mirror is approximately $0.07\text{--}0.08\text{ cm s}^{-1}$ on average; however, it is not constant. Near the end of the mirror travel, the speed decreases by 10% due to varying leaf spring tension of the mirror transport mechanism. Moreover, a 15 Hz modulation has been found in the mirror speed. It can be attributed to the mechanical interference from mechanical coolers in the AKARI satellite. The amplitude of this velocity modulation is 15% of the average velocity (see Kawada et al. 2008). As the interferograms are sampled with a frequency five times higher than the Nyquist criterion, we have sufficient oversampling to study the effect of nonuniform sampling and find that it is negligible.

³ AKARI (ASTRO-F) Observers Page - <http://www.ir.isas.jaxa.jp/ASTRO-F/Observation/>

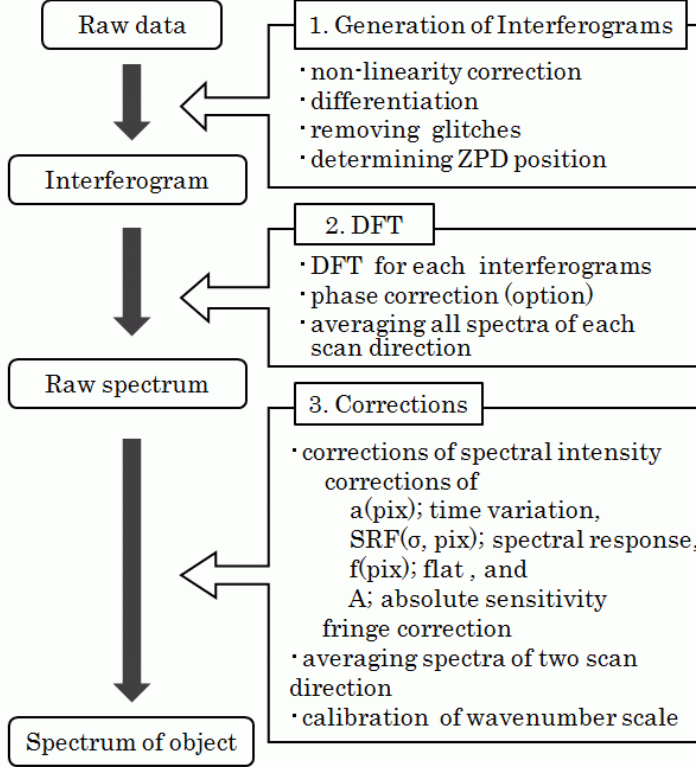


Fig. 2. Flow chart of the standard data reduction process.

FIS-FTS has a displacement sensor for the moving mirror that is used to measure the relative OPD; however, it lacks a sensor for the detection of the zero optical path difference (ZPD) position. The ZPD position is determined from the interferograms by minimizing the integral of the imaginary part of the spectra as a function of the origin of the Fourier transformation. Some examples of interferograms produced by the data processing pipeline are shown in figure 3. At this stage, the OPDs for the thermal contraction of the optical scale of the displacement sensor and the angle between the scale and the optical axis of each pixel have not been corrected. These corrections are easy and applied in the spectral domain (section 5).

3.2. Discrete Fourier Transformation (DFT)

The DFT method is adopted in the FIS-FTS data processing pipeline, which calculate a numerical integration of the associated Fourier integrals, instead of the FFT algorithm to derive better results for non-uniform sampling data. The spectra obtained at this step (hereafter, raw spectra) are calculated for each scan.

In a typical observing sequence, 11 forward and backward scans of the internal blackbody source are recorded, followed by 7 or 30 forward and backward scans of the astronomical source in the full-resolution mode or the SED mode, respectively. In the SED mode, the interferograms are double-sided with a maximum OPD of ± 0.42 cm. In the full-resolution

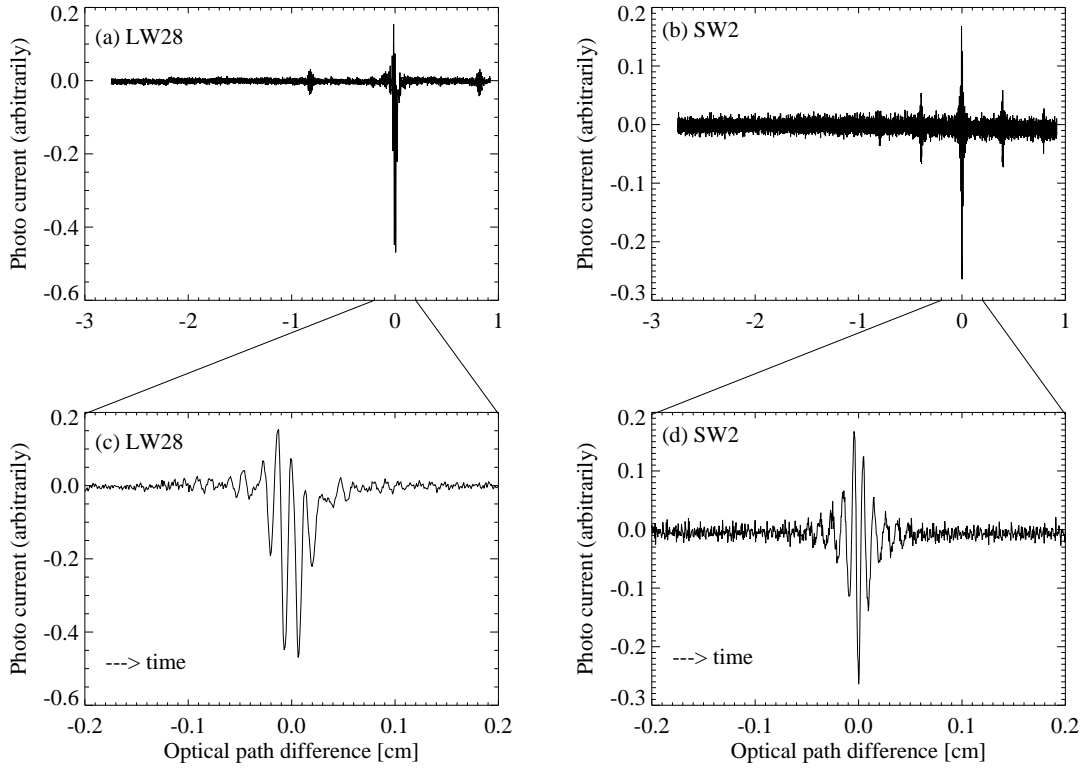


Fig. 3. Examples of interferograms measured by the FIS-FTS. Panel (a) and (b) are full range interferograms taken in the full-resolution mode of LW (LW28) and SW (SW2), respectively. Symmetric sub-structures can be seen along the optical path difference positions in both panels. Panels (c) and (d) are close-up views around the ZPD positions of panels (a) and (b), respectively. Asymmetries due to the transient response of the detectors are clearly seen.

mode, the interferogram is asymmetric, and the maximum OPD of one side is expanded to 2.7 cm and the other side to 0.9 cm. The phase information is derived from short, doubled-sided interferograms and applied to single-sided full span data to derive full resolution spectra. Since the interferograms are asymmetric in opposite directions between the forward and backward scan direction, spectra from two directions are averaged and calibrated individually.

3.3. Corrections

The raw spectrum corresponds to a product of the spectrum of the source and the total spectral response of the FIS-FTS which includes the spectral response of the detectors, the efficiency of optical filters, and the modulation efficiency of the interferometer. To derive the spectrum of the source from the raw spectrum, flat correction, correction of time variation of the detector responsivity, spectral response calibration and absolute flux calibration are required. In the case of line intensity measurements, the fringe pattern remaining in the spectrum must be removed. Finally, the source spectrum is obtained by averaging the calibrated spectra of both scan directions with the wavenumber scale correction. The derivation of these correction

factors and functions is described in sections 4 and 5.

The FIS-FTS detectors reveal the transient response (Hiromoto & Fujiwara 1999; Kaneda et al. 2002) that affects the accuracy of the measured spectra through the distortion of the interferograms. This distortion is clearly observed around the zero path position (figure 3), and varies from pixel to pixel, especially for LW. We do not attempt to correct the transient effect in time domain in this paper because of the complexity of the non-linear behavior of the photoconductive detectors. The shape of Fourier transformed spectra, within the effective wavelength range, are nearly free from the distortion of interferograms (see Kawada et al. 2008). Furthermore, since the same procedures are applied to both calibration and target source data, the effect of the transient response can be canceled as the zeroth-order approximation.

4. Correction of Spectrum

The object spectrum can be derived by the following equation as a function of both wavenumber (σ) and pixel ID (pix):

$$I(\sigma, pix) = i(\sigma, pix) \times a(pix) \times A \times f(pix) \times \frac{1}{SRF(\sigma, pix)}, \quad (1)$$

where

$I(\sigma, pix)$: the object spectrum at certain pixel [$\text{Wm}^{-2}\text{Hz}^{-1}\text{sr}^{-1}$],

$i(\sigma, pix)$: the raw spectrum [$\text{Vsec}^{-1}\text{Hz}^{-1}$],

$a(pix)$: the correction factor of the time variation of the detector responsivity at each observation,

A : the absolute flux calibration factor [$\text{W m}^{-2} \text{sr}^{-1}\text{V}^{-1}\text{sec}$],

$f(pix)$: the flat correction factor, and

$SRF(\sigma, pix)$: the relative spectral response function which includes the spectral response of both the detector and the optics.

A is a common value for all pixels while other factors a , f , and SRF are determined for each pixel independently.

We describe briefly how to derive the factors. A is derived from comparison of observed spectra of solar system objects with their models. $a(pix)$ is determined by measuring the internal blackbody source at every observation. $f(pix)$ is derived from the measurements of the aperture lid of the telescope referring to the internal blackbody source. The telescope aperture lid was measured before launch. To determine $SRF(\sigma, pix)$ of all pixels, many astronomical sources were used, whose spectra had been measured by the ISO/LWS or are well determined by models. The data used in the calibration schema are described in 4.1. The details of calibrations and fringe correction are explained in 4.2 – 4.6.

Table 2. Calibration sources.

name	mode	no. of pointed obs.	reference	flux (@100 μ m)
point source				
Uranus	SED	1 (2006/06/05 20:38)	model*	860Jy
Neptune	SED	1 (2007/05/12 22:19)	model*	340Jy
Ceres	SED	1 (2007/08/12 03:59)	model [†]	160Jy
extended source				
M82	SED	2 (2006/04/19)	ISO/LWS [‡]	$\sim 10\text{GJy sr}^{-1}$
	full-res.	7 (2006/04/19, 2006/10/22)		
Galactic center	full-res.	5 (2006/09/19, 2007/03/17-18)	ISO/LWS [‡]	$\sim 35\text{GJy sr}^{-1}$
M20	SED	1 (2006/09/23)	ISO/LWS [‡]	3–5 GJy sr ⁻¹
M17	full-res.	1 (2006/09/27)	ISO/LWS [‡]	5–37 GJy sr ⁻¹
η Carinae	full-res.	6 (2007/01/12-13, 2007/07/14)	ISO/LWS [‡]	2–8 GJy sr ⁻¹

*Müller & Lagerros (1998, 2002), [†]Moreno (1998), [‡]Archival Data

4.1. Calibration Sources

4.1.1. Astronomical Objects

Table 2 lists all the astronomical sources used for the calibration of the FIS-FTS. They are bright point sources whose fluxes are 200–900 Jy at 100 μ m or bright extended sources whose intensities are larger than a few GJy sr⁻¹. They are used to obtain the relative response function of $SRF(\sigma, pix)$ while some of the solar system objects are used for the absolute calibration of the intensity. The flux of the solar system objects changes due to their rotations and the observing geometries. The flux at the time of each observation was thus calculated using the appropriate models (Müller & Lagerros 1998, 2002; Moreno 1998). The uncertainties of the model spectra are smaller than about 5%, 20%, and 10% in the wavelength range of the FIS-FTS for Uranus, Neptune and Ceres, respectively. Uranus and Neptune were used to derive the absolute calibration factor of the FIS-FTS. These sources are frequently used as primary calibrators at far-infrared wavelengths, and Uranus was the principle calibration source for the ISO/LWS (Gry et al. 2003). Because the apparent diameters of these objects are smaller than five arcseconds, they can be considered as point sources for the FIS-FTS.

The extended sources listed in table 2 were observed by both the ISO/LWS and FIS-FTS. The calibration using these extended sources is more efficient compared to the solar system objects because many FIS-FTS pixels can be calibrated simultaneously. However, the uncertainty in the absolute intensity is larger than that derived with solar system objects, because the absolute calibration of the ISO/LWS itself has rather large uncertainty. Thus these sources are only used to derive $SRF(\sigma, pix)$.

The ISO/LWS spectroscopic observations with LWS01 (full-grating scan mode) overlap

the wavelength range covered with the FIS-FTS. Using the Off-Line Processing (OLP) version 10.1 data obtained from the ISO Archival Data Center, the LWS spectra are processed (removing glitches, averaging, defringing, and shifting to match the vertical level of the data of different detectors) using the ISO Spectral Analysis Package (ISAP⁴).

4.1.2. *The Internal Blackbody Source*

The internal blackbody source is a bright diffuse source that irradiates both of the two detector arrays and the signal-to-noise (S/N) ratio is high for almost all the pixels. However, because of its location in the instrument (figure 1), the polarity of the interferogram of the internal blackbody source is opposite to that of astronomical sources, which can induce a different distortion on the interferograms between the internal source and astronomical sources. Therefore, *SRF* cannot be made directly from the measurement of the internal blackbody source. On the other hand, since the internal blackbody source is measured at every observation, these measurements can be used to compare the on-orbit performance of the instrument with that in the laboratory before launch, and correct the time variation of the detector responsivity.

4.1.3. *Aperture Lid*

The aluminum aperture lid on top of the telescope baffle covers the entire field of the telescope in order to block radiation from the hot surface before the operation. The aperture lid could be a flat source for the array detectors. However, its extremely high temperature saturate the detectors. At the ground test of the satellite, the special aperture lid was used for the evaluation of instruments and was cooled by an extra liquid helium bath. The temperature of the cooled aperture lid is about 40 K, and all walls in the telescope cavity should be colder than the lid. The cooled aperture lid can be assumed to be a flat source because all the detector pixels see almost the same area of the lid and the scattered light from the outer area is negligible. Therefore, the measurement of the cooled aperture lid can be used as a reference for the flat-field correction.

4.2. *Correction for Time Variation*

The detector responsivity changes mainly due to the radiation environment in space. This responsivity change can be traced by measurements of the internal blackbody source at every observation. Both the measured spectral shape and the intensity are stable within 10% throughout the entire observation period of the FIS-FTS, except only for extremely high sensitivity cases that are activated by high radiation background. After scaling the detector responsivity according to the integrated signal of the internal blackbody source, the remaining variation in the spectral shapes decreases to 3–5%. The correction factor $a(\text{pix})$ is given by the ratio of the integrated signal of the internal blackbody source at each observation to the averaged value of observations.

⁴ The ISO Spectral Analysis Package (ISAP) is a joint development by the LWS and SWS Instrument Teams and Data Centers. Contributing institutes are CESR, IAS, IPAC, MPE, RAL, and SRON.

4.3. Spectral Response

The spectral response function, $SRF(\sigma, pix)$, includes all the wavenumber(σ) dependence in the flux calibration (Eq. 1) and is obtained from the ratio of the reference spectrum, $I(\sigma, pix)$, to the measured raw spectrum, $i(\sigma, pix)$, after appropriate normalization. The reference spectra are the ones from the models or ISO/LWS observations (table 2). To avoid the fringe structure in spectra described below, short span interferograms are transformed to make raw spectra. After that, the emission lines are masked and smoothed by averaging 5 points to get spectral resolution of about 6.5 cm^{-1} with better S/N ratio. Thus, $SRF(\sigma, pix)$ s obtained are shown in figure 4 as the inverse of $SRF(\sigma, pix)$. The pixel-to-pixel variation in the SW array is small enough to adopt the average as a single common SRF for all pixels as shown in panel (d). In contrast, for the LW array, $SRF(\sigma, pix)$ of each pixel is determined one by one, since the pixel-to-pixel variation of $SRF(\sigma, pix)$ is large.

The scatter of all the SRF s that are used to derive the averaged SRF described above is 5–10% for the SW array (Fig. 4d) and within 5% for the LW array in $70\text{--}85 \text{ cm}^{-1}$ (e.g., Fig. 4a-c), although it is several to 20% depending on pixels in the $60\text{--}70 \text{ cm}^{-1}$ region, where the difference in responsivity of individual pixels is relatively large.

4.4. Flat Correction

For flat correction, we use the measurement of the cooled aperture lid of the telescope (section 4.1.3) and the internal blackbody source. The measurement of the aperture lid was performed on the ground before launch, when the lid was considered to be a uniform radiator. The relative sensitivity between pixels could change after the launch as the result of changes in the effective detector bias voltage on each pixel and the radiation effects. Therefore, we cannot apply the flat correction factor derived from the measurement of the aperture lid directly to the observational data. We take spectra of the internal blackbody source both on the ground and in flight. These spectra are not completely flat but their illumination pattern is quite stable. We determine the flat correction factor in flight from the combination of the measurements of the aperture lid and the internal blackbody source.

We calculate the integrated power of derived spectra within the most sensitive wavenumber range ($70\text{--}85 \text{ cm}^{-1}$ for LW and $90\text{--}125 \text{ cm}^{-1}$ for SW) for both the aperture lid ($P_{lid,0}$) and the internal blackbody source, measured on the ground ($P_{BB,0}$) and in orbit ($P_{BB,1}$). Here, $P_{BB,1}$ is calculated for the averaged spectrum of some of the blackbody source measurement in orbit, and $P_{BB,0}$ is calculated for the spectrum measured during the same experiment of the aperture lid measurement. The flat correction factor, $f(pix)$, is determined as

$$f(pix) = P_{lid,0}(pix) \times \frac{P_{BB,1}(pix)}{P_{BB,0}(pix)}. \quad (2)$$

The first term on the right-hand represents the flat on the ground, and the second term is the correction for the sensitivity change in orbit. Figure 5 shows the distribution of $f(pix)$ for the

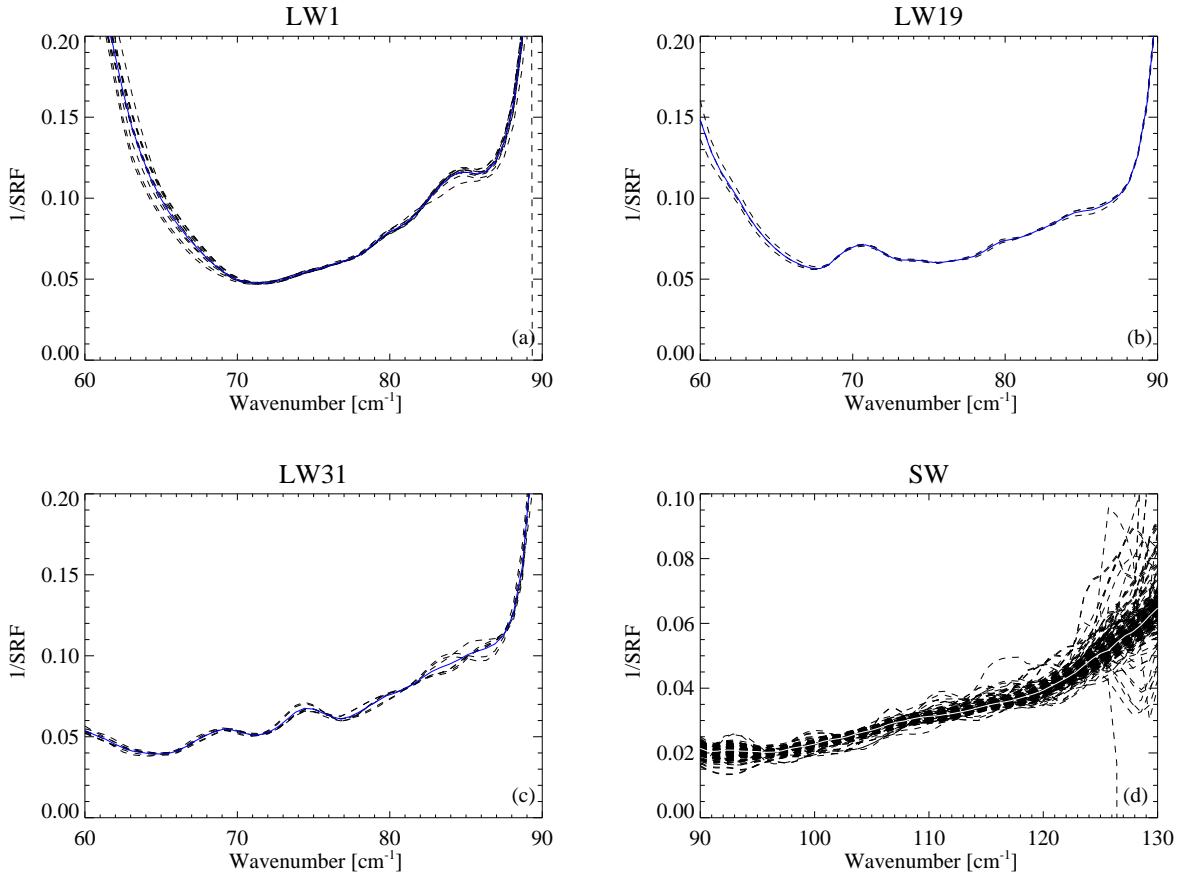


Fig. 4. Examples of *SRFs* as shown by the inverse of the *SRF* (thick solid line) with all *SRFs* before averaging. The LW pixels have a wide variety in shape as shown in panels (a) - (c). On the other hand, the SW pixels have similar shapes as shown in panel (d). The *SRF* averaged over all pixels has been adopted as the common one for the SW array.

two detector arrays. A large variation, over 10 times the responsivity in the pixels of the LW array, is observed. This variation is caused by non-uniformities in the effective detector bias voltage and in the effective spectral response (Kawada et al. 2007). Assuming that the aperture lid illuminates the array pixels with complete uniformity, the accuracy of the flat correction is around 10%, which arises from a relative calibration uncertainty due to the internal blackbody source.

4.5. Absolute Calibration

For determination of the absolute flux calibration factor A , we use the observations of Uranus and Neptune since their fluxes are accurately determined by the models (section 4.1.1) and their S/Ns are high enough. Each of them is observed only once at the appropriate position, and, thus, only two pixels of each detector can be calibrated directly. The on-pixel flux is calculated with the source position on the pixel and the point spread function of the FIS-FTS. The position uncertainty of the source on the pixel results in the uncertainty of +20%/ - 50%

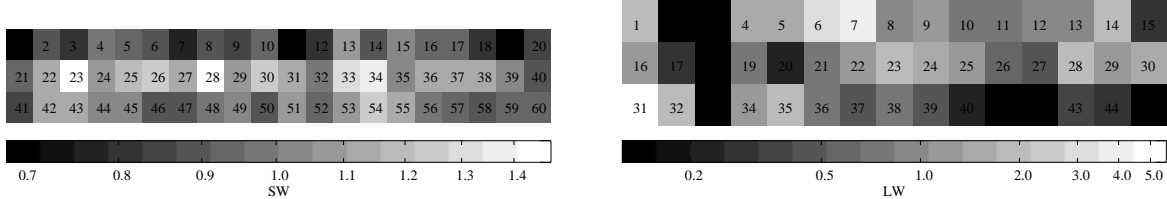


Fig. 5. Flat correction factors of SW (left) and LW (right). The gray scale indicates the relative responsiveness to the median values. Each pixel is labeled with a serial number. The pixels of SW1, SW11, LW2, LW3, LW18, LW33, and LW42 did not work in space.

in the on-pixel flux and, thus, of the factor A . This uncertainty remains the systematic error of the absolute calibration for all observations.

4.6. Fringe Correction

The interferograms of the FIS-FTS exhibit clear sub-structures that are symmetric about the ZPD (see figure 3). This pattern is called, “channel fringe”. Such features are common in Fourier spectroscopy, particularly at longer wavelengths, and associated with resonant optical cavities within the interferometer (Naylor et al. 1988). There are two different causes in the FIS-FTS: (1) multiple-beam interference between the two blocking filters, and (2) multiple-beam interference in the Ge:Ga detector substrate. Whereas the former could be seen both in LW and SW, the latter could be seen only in the SW spectra. Since the causes of the channel fringes are identified with well-defined physical properties, the features are expected to be stable and reproducible, allowing their correction using physical models.

Upon Fourier transformation the channel fringes produce an oscillatory component in the spectrum (figure 6). Since $SRFs$ are determined by using low resolution spectra ($\Delta\sigma = 6\text{--}7\text{ cm}^{-1}$), $SRFs$ do not correct the fringe pattern that appeared in the higher spectral resolution spectra. For emission line extraction, the correction of the fringe pattern is essential. A theoretical model of Airy’s formula (Born & Wolf 1975) for the resonant optical cavity is applied. The parameters of Airy’s formula are determined by fitting to several full-resolution spectra of the Galactic Center after exclusion of strong emission lines. Since the reflectivity depends on wavenumber, fitting by Airy’s formula is applied to a narrow wavenumber range around the target emission line. Two examples of the defringing spectra are shown in figure 6. After the defringing procedure, the emission lines appear clearly as shown in panels (c) and (d).

5. Scale Correction in Wavenumber

Through the preceding section, the raw values of the optical scale of the displacement sensor for the moving mirror (section 3.1) were used as the OPD. The optical scale could not

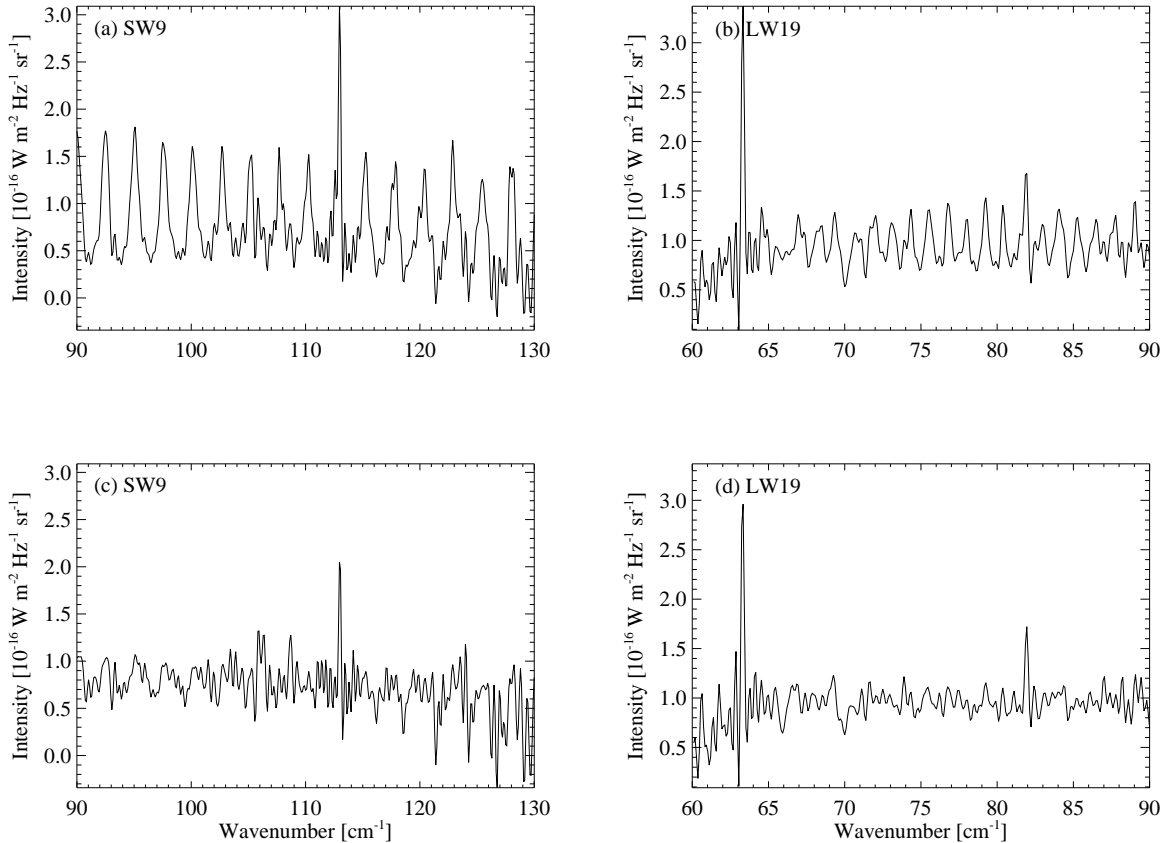


Fig. 6. Examples of the full-resolution spectra of G333.6–0.2 including emission lines. Panels (a) and (b) show the spectra of SW9 and LW19 before defringing, respectively. The fringe pattern is clearly seen in both spectra. The periodicity is different in each case as described in the text. After the defringing procedure, the emission lines appear clearly as shown in panels (c) and (d), processed from (a) and (b), respectively. The fitting ranges for the local fringe are 8 cm^{-1} in both sides around [O III] (113 cm^{-1}) in the case of panel (c) and 4 cm^{-1} in both sides around [N II] (82 cm^{-1}) in the case of panel (d). Note that there can be recognized a pattern of the sinc function at every line because the apodization is not applied.

measure the actual OPD due to the thermal shrink of the scale and declination of the alignment between the optical scale and the optical path of each pixel. The correction of these effects is expected to be given by a set of constant scaling factors, which can be determined from well measured emission lines. The observations of the Galactic Center and the Galactic Plane are suitable for determining these scaling factors because these sources are bright and have some strong emission lines in the wavenumber range of the FIS-FTS.

We fit the spectrum in the expected line profile and determine the line center in raw optical scale units. The results are shown in figure 7. Panel (a) and (b) show the line centers of the best fit values of the [N II] line (82.10 cm^{-1}) and [O III] line (113.17 cm^{-1}), respectively. Each data point indicates the median value and peak-to-peak variation of fitted line centers of all the observations (24 data points at maximum) are indicated by error bar.

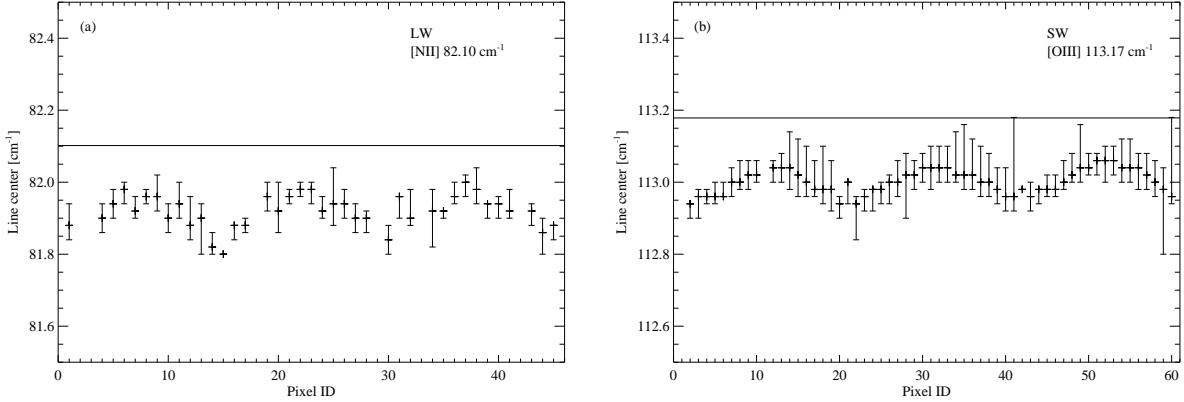


Fig. 7. Panel (a) and (b) show the line centers of the best fit values of the [N II] line (82.10 cm^{-1}) and [O III] line (113.17 cm^{-1}), respectively, which are derived from the raw values of the optical scale.

Rest frame wavenumbers of line centers are plotted by lines in each panel. Due to the thermal shrink of the optical scale, all data points are located under the lines of expected wavenumbers. We can see the common trend in figure 7 along the major axis of the detector arrays. This trend can be explained by the optical design of the FIS instrument as follows. The optical path of each pixel is not aligned with the optical axis; meanwhile, the optical scale is aligned with it. Therefore, the actual OPD of each pixel becomes longer than the measured length by the optical scale, which depends on the pixel position on the detector arrays.

Quantitatively, these shifts of line centers derived from the raw values of the optical scale are consistent with the expected values from the thermal shrink of the glass scale and the inclination of the optical path of each pixel. The [C II] line (63.40 cm^{-1}) also shows a similar trend, but with larger scatter due to its wavenumber at the step edge of the sensitivity change.

6. Evaluation of the Calibration

6.1. Accuracy of the Calibration

In this section, we summarize the absolute and relative accuracies for the continuum based on the results described in the previous sections.

As described in section 4.5, the absolute calibration accuracy of the FIS-FTS is $+20/-50\%$ for the total measured energy. In addition, the relative accuracy of the spectral response function is $\pm 10\%$ for entire spectral range of the SW. On the other hand, for LW it is $\pm 5\%$ in $70-85 \text{ cm}^{-1}$ and several to 20% in $60-70 \text{ cm}^{-1}$. Finally, we have to consider the accuracy of the flat correction, 10% , described in 4.4.

Considering all three uncertainties described above, the absolute accuracy is $+35/-55\%$ for SW, and $+35/-55\%$ in $70-85 \text{ cm}^{-1}$ and $+45/-60\%$ in $60-70 \text{ cm}^{-1}$ for LW. On the other hand, the relative accuracy among pixels of an array (the flat error) is $\pm 15\%$ for SW, and $\pm 10\%$

in 70–85 cm^{-1} and $\pm 20\%$ in 60–70 cm^{-1} for LW.

6.2. *Reproduction of some Spectra*

All the data used here are the same that were used in the calibration scheme. The evaluation of the spectra of planets that are used to make the absolute calibration will confirm the self-consistency, and the evaluation using other data will test the reliability of the calibration method. The spectra of two planets, Uranus and Neptune, and a dwarf planet, Ceres, have been derived according to the calibration procedure described in this paper. These spectra are shown in figure 8 together with empirical models. The derived spectra are in general agreement for Neptune (a) and Ceres (b). However, a clear gap in the spectrum of Uranus (c) between the SW and LW spectral range is observed. This gap, which is about 30% of the flux level, is believed to arise from the uncertainty of the flat correction and position error of the source on the pixel. If the absolute flux is scaled to match the two spectral bands, the spectral shape is accurately reproduced with the model.

7. Comparison with the ISO/LWS

We compare the FIS-FTS spectra of the extended emission from the Galactic Center region, which is observed in many pixels of the FIS-FTS and ISO/LWS. The observational results of the ISO/LWS and FIS-FTS cannot be compared directly with each other, because of the differences of the beam sizes and the observing positions. Therefore, the spectral maps are constructed in RA-DEC coordinates from the FIS-FTS data first, and then compared with the ISO/LWS results. We investigate both continuum and line emissions.

To compare the continuum flux between the ISO/LWS and the FIS-FTS measurements, integrated fluxes over the same spectral range (65–85 cm^{-1} for LW and 90–140 cm^{-1} for SW), excluding the line emission, are calculated for both spectra. The point-to-point correlation of the integrated flux between the ISO/LWS and the FIS-FTS spectra is shown in figure 9.

The ratio of the measured intensities of the FIS-FTS to those of the ISO/LWS is 0.93 on average with ± 0.07 of 1σ error for SW and 0.79 on average with ± 0.11 of 1σ error for LW. The difference is within the absolute accuracy of the FIS-FTS, +20/–50%, and that of the ISO/LWS (50%) for an extended source (Gry et al. 2003). The scatter of the data points shown in figure 9 is within the relative accuracy of the FIS-FTS, $\pm 15\%$ for SW and $\pm 10\%$ for LW.

Figure 10 shows the comparison for the line intensities measured by the FIS-FTS and by the ISO/LWS. The measured lines are the fine structure lines of [O III] 113.17 cm^{-1} , [N II] 82.10 cm^{-1} , and [C II] 63.40 cm^{-1} . The [O III] line appears in the SW spectral range, and other two lines are in LW. The average ratio of the [O III] intensity measured by the FIS-FTS to that of the ISO/LWS is 1.35 (± 0.37 in 1σ error), and [N II] and [C II] is 1.15 (± 0.27 in 1σ error). In contrast to the continuum, the line intensities measured by the FIS-FTS are systematically larger than those by the ISO/LWS, i.e., the line to continuum ratios are larger

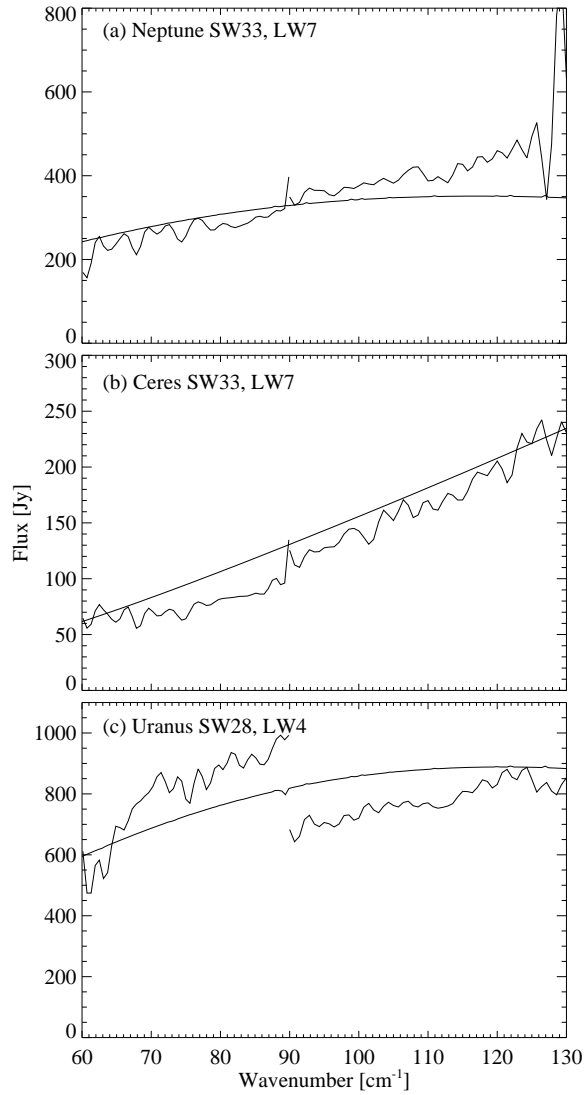


Fig. 8. Comparison between model spectra (Müller & Lagerros 1998; Müller & Lagerros 2002; Moreno 1998) and calibrated spectra according to our procedure. Three spectra are shown in panel (a) Neptune, (b) Ceres, and (c) Uranus; Neptune and Ceres were observed with the same position parameter (on-source pixel: SW33, LW7), and Uranus was observed with a different position parameter (SW28, LW4). These are reference sources used for the spectral shape and/or absolute calibration.

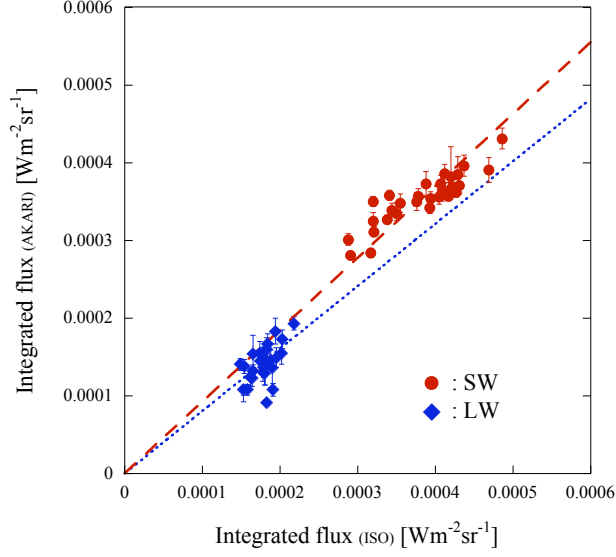


Fig. 9. Comparison of the ISO/LWS and the FIS-FTS integrated flux of the continuum emission; the wavenumber range is the same in each case. Circle and diamond symbols show data of SW and LW, respectively. The error bar of the FIS-FTS data is estimated from the discrepancy of forward and backward scan data. The dotted line and broken line represent the fitted slope for LW and SW respectively (see text).

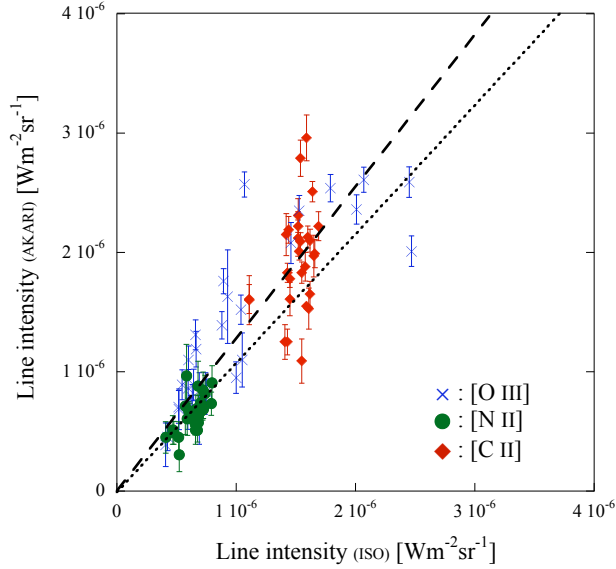


Fig. 10. Comparison of line intensities derived by the ISO/LWS and FIS-FTS. Diamond, circle, and cross symbols represent [C II] 63.40 cm^{-1} , [N II] 82.10 cm^{-1} , and [O III] 113.17 cm^{-1} lines respectively. The error bars of the FIS-FTS values indicate the fitting errors. The dotted line represents the fitted slope for LW data ([C II] and [N II]). On the other hand, the broken line represents SW data ([O III]) (see text).

than the ISO/LWS. This result may originate from the difference between Fourier transform spectrometers and grating spectrometers. In the case of Fourier transform spectrometers, the continuum intensity is dominantly determined from the modulation amplitude near the central burst, whereas the line intensities are determined from the periodic modulation of the over all interferogram. The Ge:Ga photoconductor may show non-linear behavior caused by a transient response for a large signal near the central burst of the interferogram, resulting in relatively smaller signals around the central burst. Therefore, the continuum intensity measured by a Fourier transform spectrometer may produce smaller signals relative to the line intensity. On the other hand, in the case of grating spectrometers, the line components may diffract not only to the correct position but diffusely to all positions. Therefore, the line intensities measured by grating spectrometers tend to be smaller relative to the continuum intensities if the proper absolute calibrations are not made individually.

The scattering seen in figure 10 (for the lines) is much larger than that in figure 9 (for the continuum). It is larger than the relative accuracies described in the previous section, $\pm 15\%$ for SW, and $\pm 10\%$ in $70\text{--}85\text{ cm}^{-1}$ and $\pm 20\%$ in $60\text{--}70\text{ cm}^{-1}$ for LW. For the [CII] line, the larger scatter is considered to occur because the line lies near the edge of the effective spectral range of the FIS-FTS. The [OIII] line tends to have large variation in smaller spatial scales than other lines, and thus, may be affected by the difference in the spatial resolution and the observed position of the sky between the FIS-FTS and ISO/LWS.

In summary, the continuum intensities measured by the FIS-FTS are consistent with those measured by the ISO/LWS within their absolute accuracies, $+20\% - 50\%$ for the FIS-FTS and $\pm 50\%$ for the ISO/LWS for extended sources (Gry et al. 2003). The scatter seen in figure 9 can be explained by the flat error of the FIS-FTS. On the other hand, the line intensities measured by the FIS-FTS are systematically larger than those measured by the ISO/LWS compared to the continuum emission. Based on the ISO/LWS, the line to continuum ratio of the FIS-FTS may be overestimated by 45% for both of SW and LW. The scatter seen in figure 10 is larger than that expected from the calibration error, and can be explained by small differences in the spatial resolution as well as in the observing position.

8. Conclusion

FIS-FTS operated successfully after the launch of the AKARI satellite until the supply of liquid helium expired. During its 1.5 year lifetime, the FIS-FTS acquired about 600 pointed observations. The properties of the imaging FTS equipped with photoconductive detector arrays have been presented. The calibration method discussed is based on observations of bright astronomical sources such as planets, dwarf planets, and extended sources in our Galaxy, as well as instrumental sources such as the internal blackbody source and the aperture lid. The current version of the calibration method ignores the transient response of detectors, though its effect can be seen as a distortion of the interferograms. Under this condition the relative

uncertainty of the calibration of the continuum is estimated to be $\pm 15\%$ for SW, and $\pm 10\%$ in $70\text{--}85\text{ cm}^{-1}$ and $\pm 20\%$ in $60\text{--}70\text{ cm}^{-1}$ for LW, and the absolute uncertainty is estimated to be $+35\% / -55\%$ for SW, and $+35\% / -55\%$ in $70\text{--}85\text{ cm}^{-1}$ and $+40\% / -60\%$ in $60\text{--}70\text{ cm}^{-1}$ for LW. These values are confirmed by comparison with theoretical models and previous observations by the ISO/LWS.

It should be noted that the calibration of the FIS-FTS is limited to bright sources. It is known that the transient response of detectors depends on both the background and the source fluxes. It has not been established whether the calibration presented in this paper can be extended to faint sources. A more detailed calibration study will tackle the challenging problem of the detector transient response and correct the interferograms in the time domain before the Fourier transform. It is expected that the calibration accuracy will be improved through the correction of the transient response of the detector (Kaneda et al. 2009) and the use of the larger number of lower brightness sources observed with the FIS-FTS.

AKARI is a JAXA project with the participation of ESA. We thank all the members of the AKARI project for their continuous help and support. The FIS was developed in collaboration with Nagoya University, ISAS, the University of Tokyo, the National Institute of Information and Communications Technology (NICT), the National Astronomical Observatory of Japan (NAOJ), and other research institutes. We thank ESA for financial support. We also thank Prof. R. Moreno, and Prof. T. G. Mueller for calculating the model of the solar system objects which were used for the absolute calibration.

References

- Bock, J. J., et al. 1994, *ApJ*, 410, L115
Born, M., & Wolf, E. 1975, “Principle of Optics”, Oxford Pergamon Press
Clegg, P. E., et al. 1996, *A&A*, 315, L38
Doi, Y. et al. 2002, *Adv. Space Res.*, 30, 2099–2104
Fujiwara, M., Hirao, T., Kawada, M., Shibai, H., Matsuura, S., Kaneda, H., Patrashin, M. A., & Nakagawa, T. 2003, *Appl. Opt.*, 42, 2166–2173
Griffin, M. J., & Orton, G. S. 1993, *Icarus*, 105, 53
Griffin, M., et al. 2008, *Proc. SPIE*, 7010,
Gry, C., et al. 2003, *The ISO Handbook*, vol.III: LWS – The Long Wavelength Spectrometer, version 2.1
Hiromoto, N., & Fujiwara, M. 1999, *Infrared Physics and Technology*, 40, 387
Kaneda, H., Okamura, Y., Nakagawa, T., & Shibai, H. 2002, *Advances in Space Research*, 30, 2105
Kaneda, H., et al. 2009, *PASP*, 121,549
Kawada, M., et al. 2007, *PASJ*, 59, 389
Kawada, M., et al. 2008, *PASJ*, 60, 389
Kessler, M. F., et al. 1996, *A&A*, 315, L27

- Kunde, V. G., et al. 1996, Proc. SPIE, 2803, 162
- Lim, T. L., et al. 2003, The Calibration Legacy of the ISO Mission, 481, 13
- Martin, D. H. & Puppel, E. 1969, Infrared Phys., 10, 105
- Mather, J. C., et al. 1990, ApJL, 354, L37-L40
- Mather, J. C. 1993a, Proc. SPIE, 2019, Ed. M. S. Scholl, 146–157
- Mather, J. C., Fixsen, D. J., & Shafer, R. A. 1993b, Proc. SPIE, 2019, Ed. M. S. Scholl, 168–179
- Matsuhara, H., Tanaka, M., Yonekura, Y., Fukui, Y., Kawada, M., & Bock, J. J. 1997, ApJ, 490, 744
- Moreno, R. 1998, Ph.D. Thesis. Université de Paris VI
- Müller, T. G. & Lagerros, J. S. V. 1998, A&A, 338, 340
- Müller, T. G. & Lagerros, J. S. V. 2002, A&A, 381, 324
- Murakami, H. et al. 1996, PASJ, 48, L41–L46
- Murakami, H., et al. 2007, PASJ, 59, 369
- Nakagawa, T., Doi, Y., Yui, Y. Y., Okuda, H., Mochizuki, K., Shibai, H., Nishimura, T., & Low, F. J. 1995, ApJL, 455, L35
- Naylor, D. A., Schultz, A. A. & Clark, T.A. 1988, Appl. Opt., 27, 2603
- Neugebauer, G. et al. 1984, ApJ, 278, L1–L6
- Okada, Y. et al. 2009, A&A, 514, A13
- Pilbratt, G. L. 2008, Proc. SPIE, 7010,
- Shibai, H., et al. 1991, ApJ, 374, 522
- Shibai, H., Okuda, H., Nakagawa, T., Makiuti, S., Matsuhara, H., Hiromoto, N., & Okumura, K. 1996, PASJ, 48, L127
- Shirahata, M., et al. 2009, PASJ, 61, 737
- Suzuki, T., et al. 2008, PASP, 120, 895
- Tielens, A. G. G. M. & Hollenbach, D. 1984, ApJ, 291, 722
- Verdugo, E., Yamamura, I., & Pearson, C. 2007, AKARI FIS Data User Manual, Version 1.3
- Werner, M. W., et al. 2004, ApJS, 154, 1
- Yasuda, A., Kaneda, H., Nakagawa, T., Okada, Y., Kawada, M., Murakami, N., Takahashi, H. & Ootsubo, T. 2009, PASJ, 61, 511